Materials Advances

ROYAL SOCIETY OF CHEMISTRY

PAPER

View Article Online
View Journal | View Issue

Cite this: *Mater. Adv.*, 2023, 4, 6682

Coordination-driven self-assembled Mn(II)-metallostar with high relaxivity and synergistic photothermal and photodynamic effects†

Huiyu Wu,‡[ab] Zhenghui Li,‡[ad] Yao Liu,[ac] Xingchi Shi,[e] Yuan Xue,[ac] Zuhua Zeng,[ab] Fanglin Mi,[d] Haiying Wang*[a] and Jiang Zhu *[a]

A novel Mn(II)-metallostar structure (ML_3Mn_3, M = Fe^{3+}, Ti^{4+}) was synthesized through the self-assembly of high-valence transition-metal ions (Fe^{3+} and Ti^{4+}) with a heteroditopic Mn(II) chelate (MnL) bearing a catechol group. UV-vis spectroscopy and variable-temperature ^{17}O NMR reveals pH-dependent coordination modes of the FeL_3Mn_3 metallostar, with tris-coordination at pH 9.0 and an equilibrium between tris- and bis-coordination at pH 7.4. The heteropolymetallic Mn(II)-metallostars (ML_3Mn_3) demonstrated enhanced relaxivity per Mn (more than 2-fold) compared to the monomeric Mn(II) chelate (MnL). The Fe–Mn metallostar exhibited synergistic photothermal therapy (PTT) and photodynamic therapy (PDT) effects upon 808 nm laser excitation due to ligand-to-metal charge transfer (LMCT) from the metal-catechol core, with a photothermal conversion efficiency of 20.3% and a singlet oxygen quantum yield of 24.8%. *In vitro* phototherapy studies showed that the Fe–Mn metallostar showed effective anti-tumor effects in the BxPC-3 cell line. In MRI studies in normal mice, low-dose FeL_3Mn_3 (25 μmol kg^{-1}) provided a superior contrast-enhancement compared to Gd-DTPA (100 μmol kg^{-1}) with rapid blood clearance and mixed hepatobiliary and renal excretion. In summary, we have developed a novel Mn(II)-metallostar structure with high relaxivities and synergistic NIR light-irritable PTT/PDT effects, which may be a promising theranostic agent for MRI-guided phototherapy.

Received 25th September 2023,
Accepted 13th November 2023

DOI: 10.1039/d3ma00762f

rsc.li/materials-advances

Introduction

Magnetic resonance imaging (MRI) is one of the most powerful non-invasive diagnostic tools in medical imaging, offering high spatial resolution and excellent soft-tissue contrast without ionizing radiation.[1] MRI is widely used for diagnosis, disease staging, treatment planning, and response evaluation. However, the diagnostic accuracy and confidence can be compromised when intrinsic contrast between abnormal and normal tissue is lacking. To address this, contrast-enhanced (CE) MR scanning is routinely used in clinical practice with the application of exogenous contrast agents (CAs) to enhance the contrast between lesions and surrounding normal tissues.[2]

Strong paramagnetic gadolinium (Gd^{3+}) chelates are the majority of clinically used MRI CAs, which can accelerate the longitudinal (R_1) and transverse (R_2) relaxation rates (defined as $R_i = 1/T_i$, $i = 1, 2$) of water protons in tissues, leading to increased MR signal intensity and improved imaging quality. Proton relaxivitiy (r_1 and r_2), the key parameter for evaluating the efficacy of MRI CAs, is defined as the enhancement in relaxation rate (R_1 or R_2) of water protons per mM concentration of CAs.[3] The utilization of high relaxivity contrast agents facilitates equivalent contrast enhancement at lower doses, thereby reducing the risk of systemic toxicity resulting from limited exposure.

The T_1 relaxivity of MRI contrast agents is determined by a complicated interplay of various molecular parameters that govern the magnetic dipolar interactions between water

[a] *Medical Imaging Key Laboratory of Sichuan province, Department of Oncology, Affiliated Hospital of North Sichuan Medical College, Maoyuan Road 1, Nanchong City, Sichuan, 637000, China. E-mail: hywang@nsmc.edu.cn, zhujiang@nsmc.edu.cn*
[b] *School of Pharmacy, North Sichuan Medical College, Fujiang Road 234, Nanchong City, Sichuan, 637000, China*
[c] *School of Basic Medical Sciences and Forensic Medicine, North Sichuan Medical College, Fujiang Road 234, Nanchong City, Sichuan, 637000, China*
[d] *Department of Stomatology, North Sichuan Medical College, Fujiang Road 234, Nanchong City, Sichuan, 637000, China*
[e] *Department of Cardiovascular Disease, School of Clinical Medicine, Affiliated Hospital of North Sichuan Medical College, Maoyuan Road 1, Nanchong City, Sichuan, 637000, China*

† Electronic supplementary information (ESI) available: Photographs of the aqueous solutions, photographs at different pH conditions, the molar absorption coefficient (ε), stability in different mediums, photothermal conversion efficiency, $^1O_2$ quantum yield and hyperthermia heating curves of BxPC-3 cell media for FeL_3Mn_3 at 808 nm, and an ascorbate shielding effect for the photodynamics of FeL_3Mn_3 metallostars. See DOI: https://doi.org/10.1039/d3ma00762f

‡ These authors contributed equally.

protons and unpaired electrons on the paramagnetic metal center. The following three factors are the main contributors: the number of water molecules directly coordinated to the metal center (q), the residence time of the coordinated water molecule (τ_m), and the rotational correlation time (τ_R) representing the inverse of the molecular tumbling rate of the complex in solution.[4]

The rapid molecular tumbling of clinically used small molecule Gd-based contrast agents (GBCAs) in solution, with a rotational correlation time (τ_R) on the order of tens of picoseconds, does not match the clinically relevant Larmor frequencies (<3.0 T, 127 MHz). As a result, GBCAs exhibit low relaxivity (in the range of 3–4 mM^{-1} s^{-1}, at 0.47 T and 37 °C), which was far below their theoretically possible value.[4,5]

In order to obtain high relaxivity contrast agents, efforts have been made to made to optimize τ_R by conjugating Gd(III) complexes to nanoparticles,[6] and macromolecular architectures[7] (proteins,[8,9] plolymers,[10–12] and dentrimers[13–15]) to slow the rotation motion of the agent in solution.[16]

Supramolecular architectures, known as 'metallostar', represent another effective approach for obtaining high per Gd relaxivity contrast agents. This approach relies on the coordination-driven self-assembly of heteroditopic Gd(III) chelates in a rigid and compact space around a suitable central d- or p-block metal ion. The formation of supramolecular architectures in a rigid and compact space allows for the optimization of multiple sets of parameters related to molecular motion in solution. For example, increasing the molecular weight while restricting free rotation of the Gd center can be achieved simultaneously (see Chart 1).

Gd-metallostars, as pioneered by Toth, Merbarch, Desreux and others, are based on various heteroditopic ligands that incorporate two different complexing moieties, such as standard polyaminocarboxylate-based ligands for Gd(III) and diverse bidentate or tridentate ligands for central transition metal ions (Al(III), Ti(IV), Fe(II), Co(II), Ni(II), Ru(II), and Cu(II)) including derivatives of bipyridine, terpyridine, 8-hydroxylquinoline, phenanthroline, dipicolinic acid, and dithiocarbamate and catechol (Chart 1).[17–19]

In recent years, the safety of GBCAs has been questioned due to the emergence of nephrogenic systemic fibrosis (NSF)[20,21] and brain gadolinium retention,[22–24] triggering investigation into alternatives to Gd-based CAs. In particular, good biocompatible Mn(II)-based chelates with excellent thermodynamic stability and kinetic inertness have been designed and developed as contrast agents.[25,26]

However, small molecule manganese-based contrast agents (MBCAs) also suffer from low relaxivity for the same reasons as

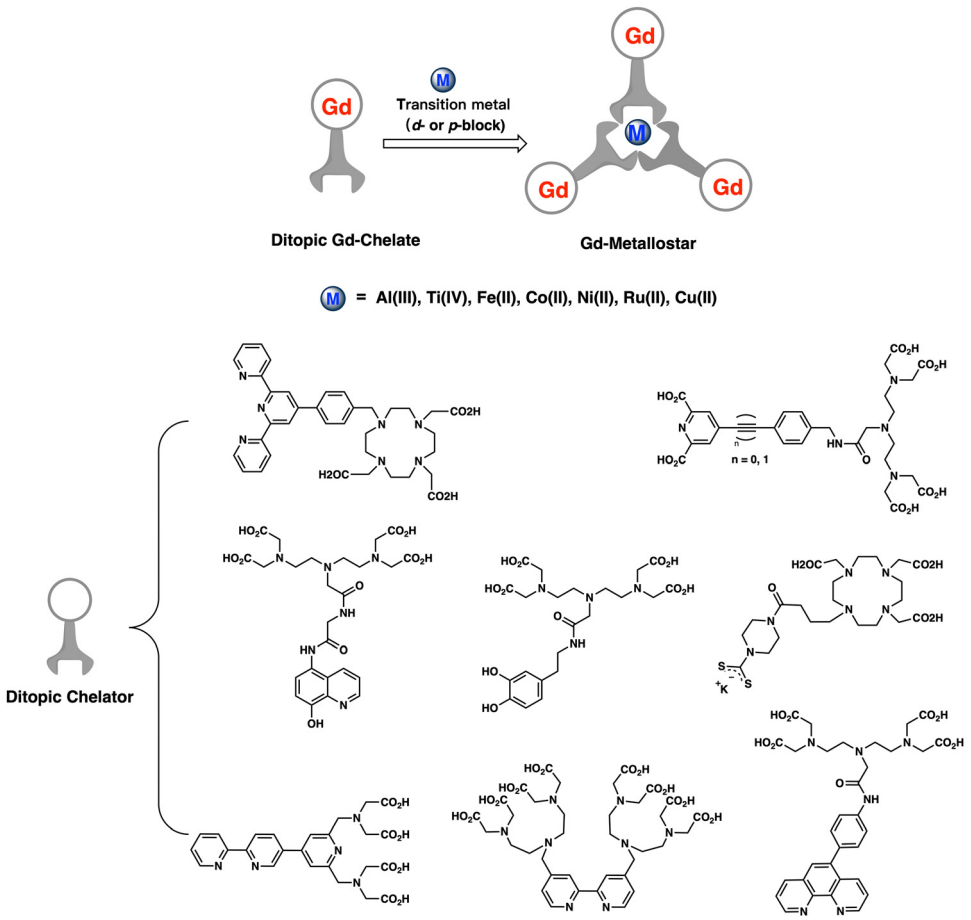

Chart 1 Schematic diagram of the structure of Gd-metallostars (ML_3Gd_3).

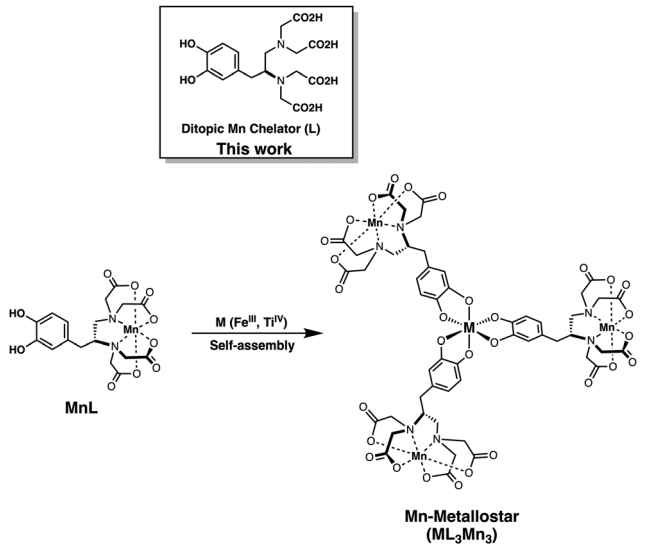

Chart 2 The structures of ditopic ligand (L), heteroditopic Mn(II) chelate (MnL), and Mn-metallostar (ML_3Mn_3) discussed in this paper.

clinically used GBCAs, as discussed above. Moreover, Mn(II) (S = 5/2) is less paramagnetic compared to Gd(III) (S = 7/2). In this context, by taking advantage of the established metal-catecholate chemistry,[27–29] we designed a novel Mn(II)-metallostar contrast agent in which three Mn(II) complexes are assembled around high-valence transition metal (Fe(III), Ti(IV)) ions to form a tetrametallic species (ML_3Mn_3). As shown in Chart 2, the ditopic ligand (L) derived from L-Dopa contains an EDTA moiety and a catechol group, serving as the complexing unit for the Mn(II) ion and transition metal ions (M = Ti^{4+} or Fe^{3+}), respectively.

Additionally, as demonstrated in precedent studies like in the Fe(III)-Tiron system,[30] the Fe(III)-catechol core can provide a relatively intense and broad absorption band in the visible to near-infrared (NIR) region due to ligand-to-metal charge transfer (LMCT) and ligand-localized π–π* electronic transitions, providing this Mn(II)-metallostar with potential for NIR-responsive phototherapy properties.

Phototherapy, including photothermal therapy (PTT) and photodynamic therapy (PDT), has emerged as a promising therapeutic modality for cancer in recent years. It has attracted increasing attention due to its advantages of non-invasiveness, low side effects, and remote controllability.[31–35] Irritation light in windows I and II of NIR ranging from 650 to 950 and 1000 to 1350 nm, respectively, possess remarkable benefits, including deeper penetration of biological tissue, less tissue scattering and absorption, and low photo-damage. Therefore, photosensitizers that can be irritated in the so-called biological transparency windows (NIR I and NIR II) are highly desired for achieving efficient phototherapy *in vivo*.

Based on the attractive properties of high relaxivity and NIR optical absorption of the metallostar structure discussed above, herein we report the synthesis and characterization of a new type of Mn(II)-metallostar (ML_3Mn_3, Chart 2). This metallostar exhibits high per Mn relaxivities and NIR-responsive synergistic effects of PTT and PDT, making it an attractive theranostic agent for MRI-guided phototherapy.

Results and discussion

Synthesis and characterization

The synthesis of the catechol-EDTA-based ligand (L) and the corresponding Mn(II) complex (MnL) was described in our previous study for the development of a $T_1 - T_2$ dual-modal MRI contrast agent based on superparamagnetic iron oxide nanocrystals with a surface coated with MnL.[36] In the present study, saturated tris-coordination Mn(II)-metallostars (Mn: M = 3 : 1, M = Fe(III), Ti(IV)) were prepared at pH = 8.5 due to the presence of the mixed coordination form of bis and tris-coordination complexes at pH < 7.8 when Fe(III) was used as the central metal ion.[37]

With the addition of iron(III) acetylacetonate ($Fe(acac)_3$) or titanium(IV) oxide acetylacetonate ($TiO(acac)_2$) to MnL aqueous solution, the color of the solution changed from light yellow to purple-black or orange-red, respectively. Pronounced changes in the color of the above reaction solutions indicated the coordination of the catechol group with metal ions.[38] Pure dark violet (Fe(III)) or orange-red (Ti(IV)) solid products were precipitated from the aqueous solution by adding isopropyl alcohol or acetone. High-resolution mass spectrometry (HRMS, ESI^+) revealed significant peaks at 1455.0683 and 1446.0740 m/z (Fig. 1), in good agreement with the calculated mass of H^+ adducts $[C_{51}H_{48}Mn_3FeN_6O_{30}H_{10}]^+$ (1455.0684 m/z) and $[C_{51}H_{48}Mn_3TiN_6O_{30}H_9]^+$ (1446.0741 m/z), respectively. The results confirmed a 3 : 1 ratio of Mn^{2+} *versus* Fe^{3+}/Ti^{4+} in these complexes. Therefore, the structure of the metallostars can be represented as FeL_3Mn_3 or TiL_3Mn_3.

Photophysical study

Water solubility is high for all three complexes (MnL, TiL_3Mn_3 and FeL_3Mn_3) and their aqueous solutions exhibit lavender, yellow and blue colors, respectively (Fig. S1, ESI†). The absorption spectrum of aqueous solutions of MnL, TiL_3Mn_3 and FeL_3Mn_3 (in HEPES buffer, pH = 7.4, 0.1 M) is shown in Fig. 2(a). The characteristic strong absorption peaks of MnL and TiL_3Mn_3 located at 281 nm are attributed to the n–π* and π–π* intra-ligand electronic transitions, while a slight red-shift to 289 nm is seen for FeL_3Mn_3. In addition, due to the presence of ligand-to-metal charge transfer (LMCT) in the 3d metal-catecholate structure in the Mn(II)-metallostar core, new broader absorption bands were observed for metallostars than for monomeric MnL, ranging from 400 to 850 nm for FeL_3Mn_3 and 350 to 550 nm for TiL_3Mn_3 (Fig. 2a). Therefore, the low-energy LMCT absorption band extending into the near-infrared (NIR) region makes FeL_3Mn_3 a potential photosensitizer for exploring the photothermal/photodynamic effects triggered by single-wavelength NIR light (808 nm) and the performance of TiL_3Mn_3 will not be discussed further in this study.

As reported by Nucera *et al.*[30] and Charkoudian *et al.*,[37] Fe(III)-catechol (Cat) type complexes demonstrated pH-dependent

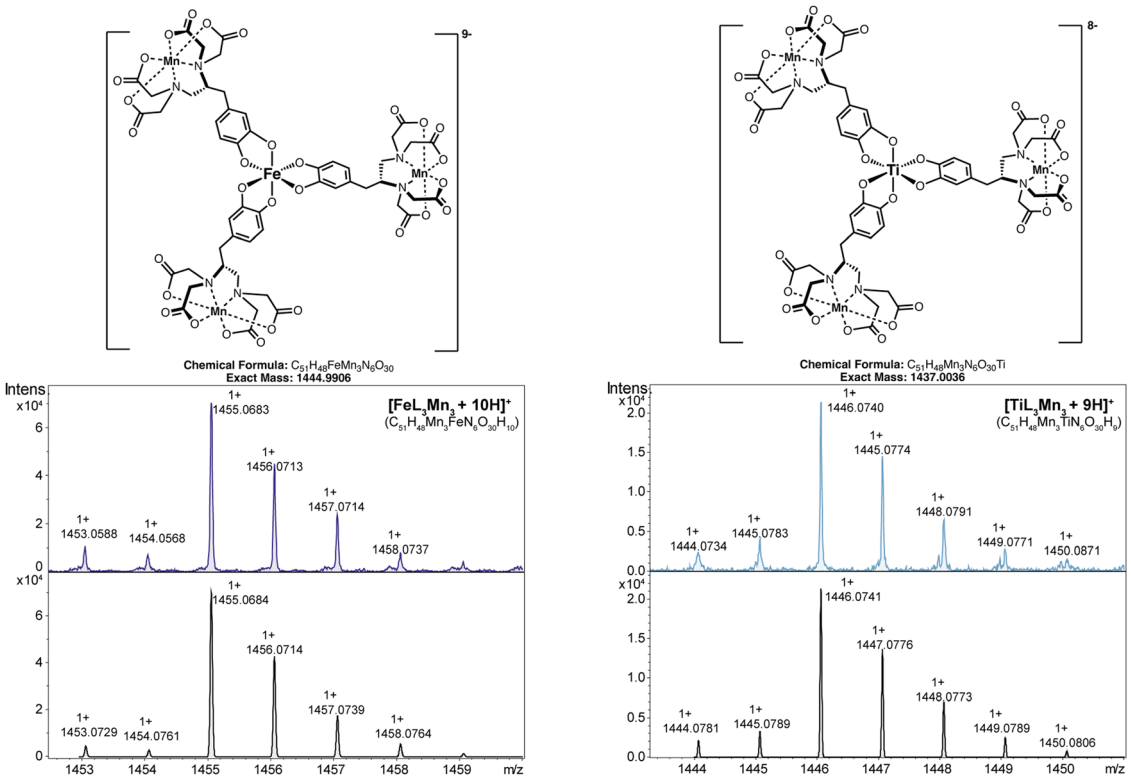

Fig. 1 Measured and calculated isotope distribution for the single charged ions of FeL_3Mn_3 and TiL_3Mn_3 (high resolution mass (HRMS, ESI^+)).

coordination equilibria, existing as mono-, bis-, and tris-Cat coordination forms with different Fe(III)-hydrated states ($[Fe(Cat)_x(H_2O)_{6-2x}]$, x = 1, 2, 3) when the pH varied from acidic to alkaline values. In this work, as shown in Fig. 2(b)

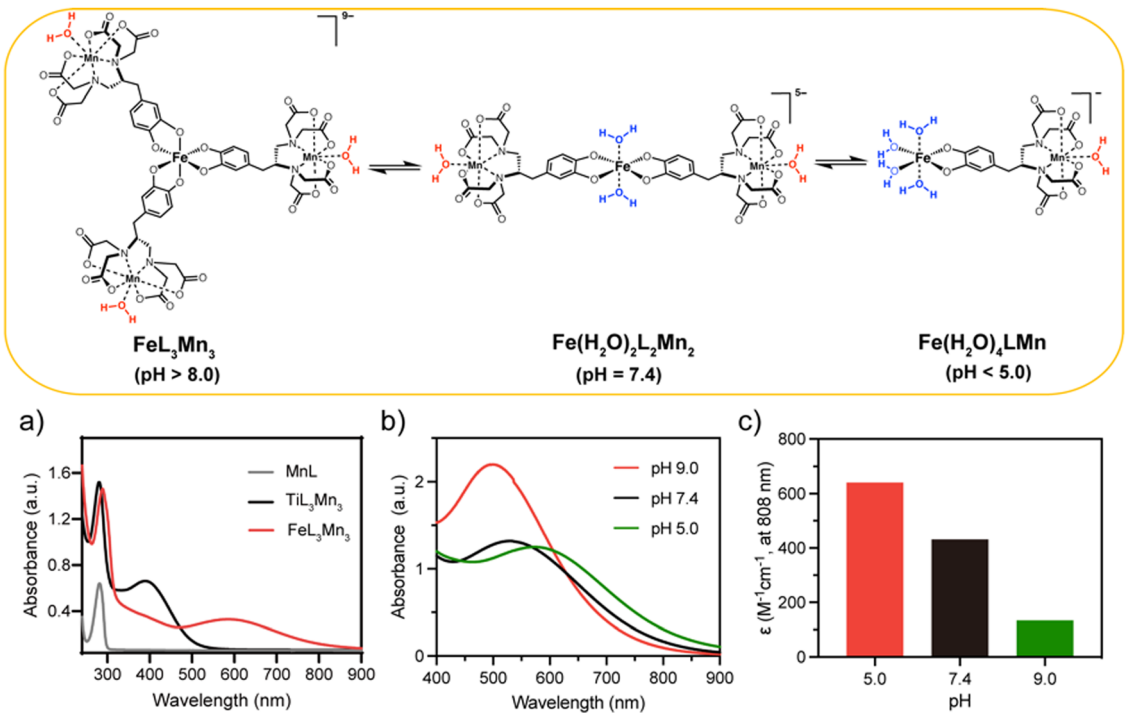

Fig. 2 The tri-/bis-coordination equilibrium of the Fe(III)–Mn(II) metallostar and photophysical properties of MnL, TiL_3Mn_3 and FeL_3Mn_3. (a) Absorption spectra of the prepared MnL, TiL_3Mn_3 and FeL_3Mn_3 solutions (0.063 mM, in HEPES buffer, pH = 7.4, 0.1 M). (b) Absorption spectra of FeL_3Mn_3 (0.42 mM) at pH = 5.0, 7.4 and 9.0 (in Tris buffer, 0.1 M). (c) Molar absorption coefficient (ε) of FeL_3Mn_3 at 808 nm at pH = 5.0, 7.4 and 9.0 (in Tris buffer, 0.1 M).

(and Fig. S2, ESI†), the tris-coordinated FeL_3Mn_3 (λ_{max} ~ 493 nm) predominated at pH > 8.0, while the bis-coordinated [$FeL_2Mn_2(H_2O)_2$] (λ_{max} ~ 530 nm) and mono-coordinated [$FeLMn(H_2O)_4$] (λ_{max} ~ 600 nm) are predominant in the pH range of 5.0–7.0 and at pH < 5.0, respectively. At pH 7.4, the Mn-metallostar system existed as an equilibrium of tris-/bis-coordination species, with heavy overlap in their absorption spectrum from ~400–620 nm.

Interestingly, the pH-dependent optical absorption displayed by the Fe(III)–Mn(II) metallostar is analogous to that of the Fe(III) complex (Fe-ZDS) reported by Liang *et al.*[39] As depicted in Fig. 2(c), the molar absorption coefficient of metallostar at 808 nm varies significantly with values of 641, 432 and 134 M^{-1} cm^{-1} at pH 5.0, 7.4 and 9.0, respectively. This pH-responsive optical absorption could facilitate precise photothermal tumor therapy, since it enables selective activation of the photothermal effect in the acidic tumor microenvironment,[40] minimizing damage to normal cells. Moreover, FeL_3Mn_3 exhibited good stability in FBS solution or PBS solution (Fig. S3, ESI†), suggesting that FeL_3Mn_3 is promising for *in vivo* MR imaging.

Variable-temperature ^{17}O-NMR study

Variable-temperature ^{17}O-NMR is a powerful technique to directly probe the coordination environments including the hydration state and dynamic parameters of paramagnetic complexes of interest for MRI applications.[41] For Mn(II) complexes, the observed maximum water ^{17}O transverse relaxivity (r^O_{2max}, mM^{-1} s^{-1}) is extremely sensitive to the number of inner-sphere water ligands (q) coordinated to the Mn(II) ion ($q = r^0_{2max}/510 \pm 100$ mM^{-1} s^{-1}).[42] As shown in Fig. 3, the Fe–Mn Metallostar at pH 9.0 has a temperature-dependent r^0_2 curve similar to that of monomeric MnL, with the measured r^0_{2max} values of 450 and 480 mM^{-1} s^{-1}, respectively. This revealed a tris-coordinated form for metallostar ([FeL_3Mn_3]) with one bound water on Mn(II) and no hydration on Fe(III) at pH 9.0. However, an increased r^0_2 for the metallostar with an r^0_{2max} of 560 mM^{-1} s^{-1} was observed within the same temperature range at pH 7.4. This may indicate the equilibrium of tris-/bis-coordination forms for metallostar at pH 7.4 and a hydrated state of Fe(III) center with two bound water molecules in the bis-coordinated form ([$FeL_2(H_2O)_2Mn_2$]).

Therefore, the combination of the ^{17}O NMR and UV-vis experiments provides definitive evidence that the metallostar adopts a tris-coordinated form at pH 9.0 and an equilibrium between tris-and bis-coordination at pH 7.4 (Fig. 2).

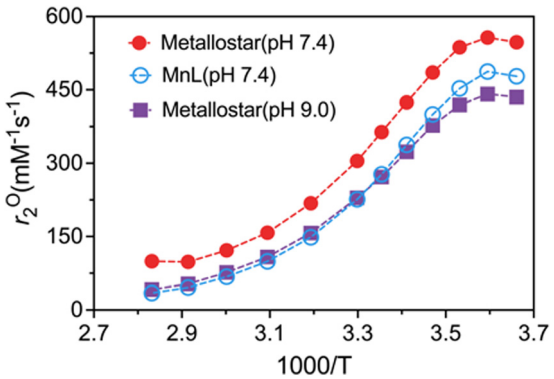

Fig. 3 Variable-temperature ^{17}O NMR studies of monomeric MnL and Fe(III)–Mn(II) metallostar at pH 9.0 and 7.4.

Relaxometric study

In HEPES buffer (pH = 7.4, 0.1 M) and at 0.47 T, 32 °C, the per paramagnetic metal ion relaxivities (r_1) of the metallostars FeL_3Mn_3 and TiL_3Mn_3 were determined to be 6.06 and 7.87 mM^{-1} s^{-1}, respectively. This is substantially higher than the r_1 of the monomeric MnL (3.66 mM^{-1} s^{-1}). The lower r_1 of the Fe–Mn metallostar compared to the Ti(IV) analogue suggests the Fe(III) center exhibits an equilibrium between tris-and bis-coordination (lower molecular weight) at pH 7.4 based on the pH-dependent coordination chemistry elucidated by NMR and UV-vis spectroscopy. In contrast, the Ti–Mn metallostar maintains a high molecular weight ML_3Mn_3 structure at pH 7.4, consistent with its higher per paramagnetic metal ion relaxivity. In addition to the improved relaxivities, the observed low r_2/r_1 ratio close to 1.00 (1.19 for FeL_3Mn_3 and 1.25 for TiL_3Mn_3) indicated that Mn-metallostars are favorable T_1 agents for T_1-weighted imaging.

Compared to the relaxivities of the tri-/bis-coordination equilibrium system of the Fe(III)–Mn(II) metallostar measured at pH = 7.4 (in HEPES buffer, 0.1 M), tris-coordination FeL_3Mn_3 (pH = 9.0, in Tris buffer, 0.1 M) showed reduced relaxivity (r_1 = 5.29 mM^{-1} s^{-1} and r_2 = 6.83 mM^{-1} s^{-1}). The relaxivity changes can be attributed to the different hydrated states of the Fe(III) center in bis- and tri-coordination of Fe(III)–Mn(II) metallostar. Specifically, two-water molecules coordinate to the Fe(III) center in the bis-coordinated form, while no water molecule coordinates in the tris-coordinated form of the Fe(III)–Mn(II) metallostar (Fig. 2 and Table 1).

Photothermal effect of Fe–Mn metallostar

The NIR absorption of the Fe–Mn metallostar enables us to systematically investigate its photothermal effect with varying FeL_3Mn_3 concentration and laser power density under 808 nm. Fig. 4(a) shows infrared thermographs of the temperature elevation for Fe–Mn metallostar solution at different concentrations (in HEPES buffer, pH = 7.4, 0.1 M) irritated at a fixed laser power density (2.0 W cm^{-2}). Under these conditions,

Table 1 A comparison of relaxivities (r_1 and r_2) for Mn(II) monomer and metallostars (ML_3Mn_3, M = Fe^{3+}, Ti^{4+}) (in HEPES buffer, pH = 7.4, 0.1 M, at 0.47 T, 32 °C)

	Relaxivities		
Sample name	r_1[a] [mM^{-1} s^{-1}]	r_2[a] [mM^{-1} s^{-1}]	r_2/r_1
MnL	3.66	4.99	1.36
Fe–Mn metallostar	6.06 (5.29[b])	7.19 (6.83[b])	1.19 (1.29[b])
TiL_3Mn_3	7.87	9.87	1.25

[a] The mM represents concentrations of paramagnetic metal ions. [b] In Tris buffer (pH = 9.0, 0.1 M).

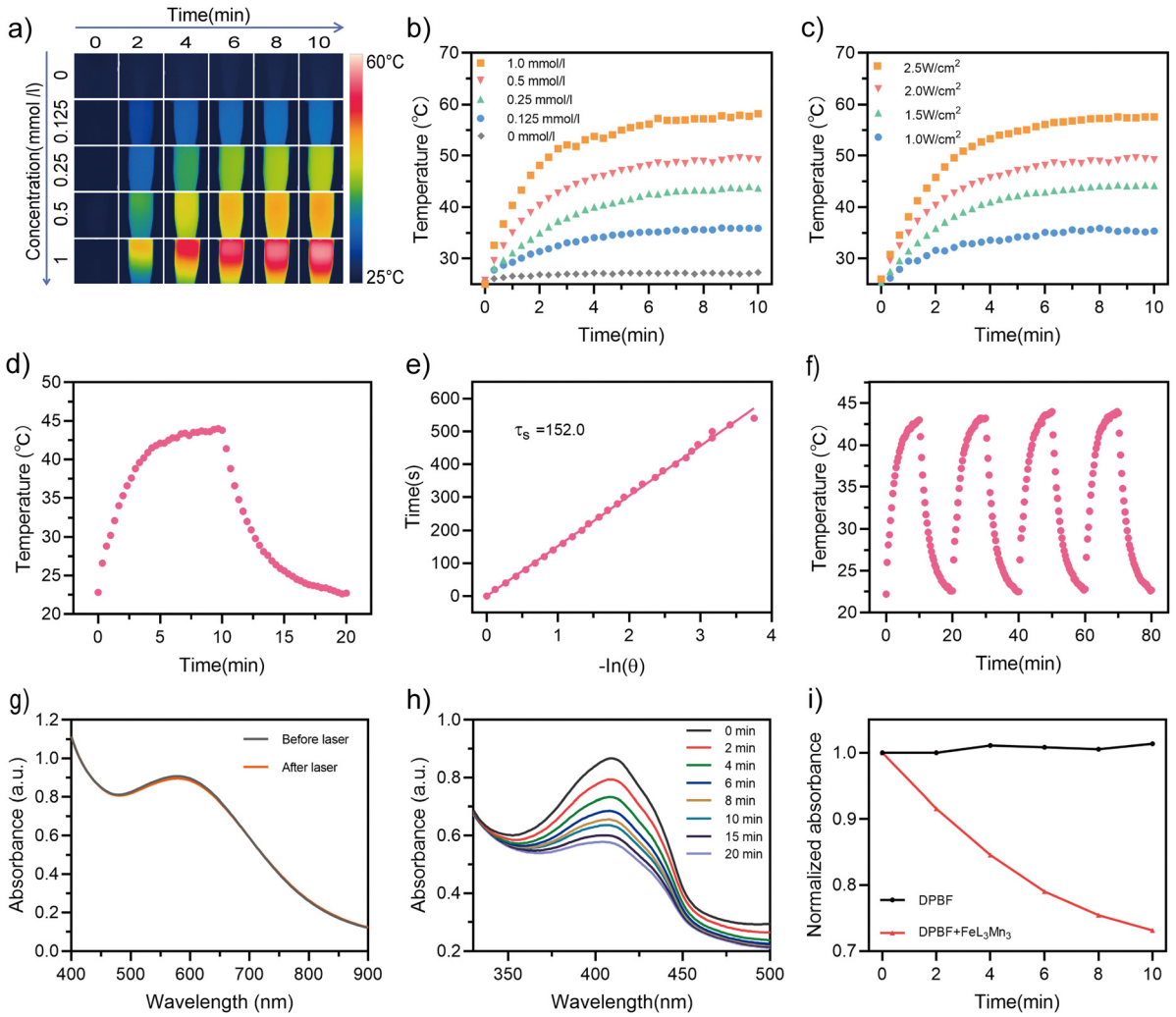

Fig. 4 Photothermal and photodynamic effects of Fe–Mn metallostar. (a) The thermal images and (b) photothermal heating curves of FeL_3Mn_3 in HEPES buffer (pH = 7.4, 0.1 M) with various concentrations under 808 nm laser (2 W cm^{-2}) irritation. (c) Photothermal heating curves of Fe–Mn metallostar (0.5 mM) in HEPES buffer (pH = 7.4, 0.1 M) under 808 nm laser irritation at various laser power densities. (d) Fe–Mn metallostar (0.25 mM) was irradiated (808 nm, 2 W cm^{-2}) for 10 min to reach a temperature plateau, and cooled naturally for 10 min to room temperature without irritation. (e) Linear correlation of cooling times *versus* driving force temperature for Fe–Mn metallostar. (f) Photothermal stability of Fe–Mn metallostar (0.25 mM) after four cycles of heating and cooling (808 nm, 2 W cm^{-2}). (g) Absorption spectra of Fe–Mn metallostar before and after of laser on/off irritation. (h) The change of absorption spectra of DPBF (20 μM) mixed with Fe–Mn metallostar (80 μM) over time under 808 nm laser irritation (1.5 W cm^{-2}). (i) Normalized absorbance at the 410 nm characteristic peak of DPBF and DPBF mixed with Fe–Mn metallostar under laser irritation (808 nm, 1.5 W cm^{-2}) over time.

when irritated for 10 minutes, the heating curves showed a concentration-dependent photothermal effect with a maximum temperature increment of 23.4 °C for the 0.5 mM Fe–Mn metallostar solution compared to 1.6 °C for the control solution without photosensitizer (Fig. 4b). As Fig. 4(c) indicates, the heating curves also showed a laser power-dependent photothermal effect with the highest temperature reaching 57.6 °C under an NIR (808 nm) laser power density of 2.5 W cm^{-2} when the Fe–Mn metallostar concentration was set to 0.5 mM.

To assess the photothermal performance, we exposed the Fe–Mn metallostar solution (0.25 mM) to laser irritation (808 nm, 2.0 W cm^{-2}) for 10 min until it reached a temperature plateau, and then allowed it to cool naturally for 10 min until it returned to room temperature (Fig. 3d). The photothermal conversion efficiency (η) was calculated to be 20.3% using the reported method.[43] The time constant was obtained using a linear regression curve between the cooling stage and the negative natural logarithm of the thermal driving force temperature of the solution (Fig. 4e).

In addition, under on–off 808 nm laser irritation (2.0 W cm^{-2}), the Fe–Mn metallostar solution temperature maintained a coincident reciprocation of the rising and cooling process (Fig. 4f), suggesting the excellent photothermal stability of FeL_3Mn_3. This was further confirmed by the negligible changes in the absorption spectrum measured before and after on–off 808 nm laser irritation (Fig. 4g).

Singlet oxygen-generating capability of Fe–Mn metallostar

Given the intense LCMT band (600–800 nm) and the excellent photothermal stability of Fe–Mn metallostar, we further

explored its efficacy as a NIR light photodynamic therapy (PDT) agent. In this study, 1,3-diphenylisobenzofuran (DPBF) was used as a singlet-oxygen ($^1O_2$) trapping agent to evaluate the ability of Fe–Mn metallostar to produce $^1O_2$ by monitoring the change in the absorption intensity at 410 nm.[44,45] As shown in Fig. 4(h) and (i), the degradation rate of DPBF exhibited a linear positive correlation with the irritation time (808 nm, 1.5 W cm^{-2}), indicating that $^1O_2$ generated by FeL_3Mn_3 can continuously consume DPBF when exposed to laser light. In addition, the $^1O_2$ quantum yield was calculated to be 24.8% using indocyanine green (ICG) (Φ_Δ = 0.14 in water)[46] as the standard reference (Fig. S5, ESI†).[47]

Photocytotoxicity on BxPC-3 cells

Encouraged by Fe–Mn metallostar's promising synergistic PTT and PDT effects, we investigated its photocytotoxicity effect on the BxPC-3 cell line. As shown in Fig. S6 (ESI†), in the cell culture medium loaded with 0.5 mM Fe–Mn metallostar, the temperature rapidly increased by 28.6 °C over 6 minutes of 808 nm laser irradiation (2 W cm^{-2}), whereas it only increased by 2.7 °C in the absence of Fe–Mn metallostar. These results suggested that Fe–Mn metallostar could effectively produce photocytotoxicity with a large amount of heat combined with ROS ($^1O_2$) to induce cell death under 808 nm laser irritation.

Indeed, the phototherapy effect of Fe–Mn metallostar was confirmed by *in vitro* dark cytotoxicity and photocytotoxicity tests (Fig. 5a). CCK-8 assays showed that Fe–Mn Metallostar had low cytotoxicity and excellent biocompatibility, with cell viability higher than 90% after 24 h of incubation in the dark with up to 500 μM Fe–Mn metallostar alone. However, when 250 μM of Fe–Mn metallostar was loaded and irritated under 808 nm laser light at a power density of 2.0 W cm^{-2}, Fe–Mn metallostar induced dose-dependent cell death and the survival rate was close to zero (Fig. 5a).

To further clarify the relative contributions of photothermal and photodynamic effects to the cytotoxicity, two control experiments were performed. To investigate the photodynamic effect alone, the environmental temperature was maintained at 4 °C using an ice bath to suppress hyperthermia. To study the photothermal effect alone, sodium ascorbate was added to scavenge singlet oxygen to shield the photodynamic effect (Fig. 5a and Fig. S7, ESI†). These control experiments suggested Fe–Mn metallostar can generate synergistic photodynamic and photothermal cytotoxic effects, while the photothermal effect on BxPC-3 cells was more potent than the photodynamic effect under the conditions tested.

The occurrence of rapid cell death induced by phototoxicity was further confirmed by the live/dead cell staining assay, in which only the Fe–Mn metallostar-loaded group irritated with an 808 nm laser showed significant cell death when living cells were stained with calcein acetoxymethyl ester (calcein-AM, green fluorescence) and the dead cells were stained with propidium iodide (PI, red fluorescence) (Fig. 5b).

MR imaging study

The results above suggest that FeL_3Mn_3 holds great promise as a theranostic agent for MR imaging-guided phototherapy based on its high relaxivity per Mn ion and NIR responsive synergistic PTT/PDT effects. Finally, we conducted *in vivo* MRI studies in normal mice to evaluate the contrast enhancement, distribution, and elimination of FeL_3Mn_3 compared to the commercially available Gd-DTPA. During the arterial phase (1 min post-injection) as shown in Fig. 6(a), a low-dose of Fe–Mn metallostar (25 μmol kg^{-1}) produced strong intravascular contrast enhancement, with the heart, carotid arteries, abdominal aortal, and renal arteries more clearly delineated compared to Gd-DTPA (100 μmol kg^{-1}). Dynamic MR imaging showed that Fe–Mn metallostar undergoes a combination of renal and hepatobiliary clearance, with significant enhancements of the bladder and gallbladder observed at 5 min and 20 min post-injection, respectively. Fig. 6(b)–(d) depict the change in normalized signal-to-noise (nSNR) for the heart (blood), liver, and kidney within 30 min post-injection, indicating a low-dose of FeL_3Mn_3 produced better enhancement in the heart (blood),

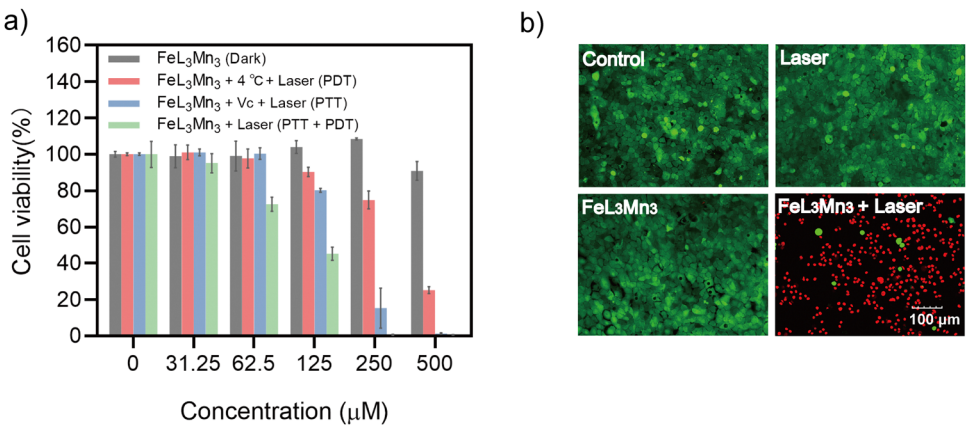

Fig. 5 Cellular biocompatibility and NIR-irritated phototoxicity study for FeL_3Mn_3. (a) Cell viabilities of BxPC-3 cells incubated with different concentrations of Fe–Mn metallostar under different experimental conditions (without or with irradiation (NIR = 808 nm, 2 W cm^{-2}, 10 min); 4 °C was used to suppress the PTT effect and Vitamin C was used to shield the PDT effect). (b) Fluorescence images of Calcein AM (green fluorescence; live cells) and PI (red fluorescence; dead cells) co-stained BxPC-3 cells with different treatments (NIR = 808 nm, 2.0 W cm^{-2}, 10 min, FeL_3Mn_3 = 500 μM).

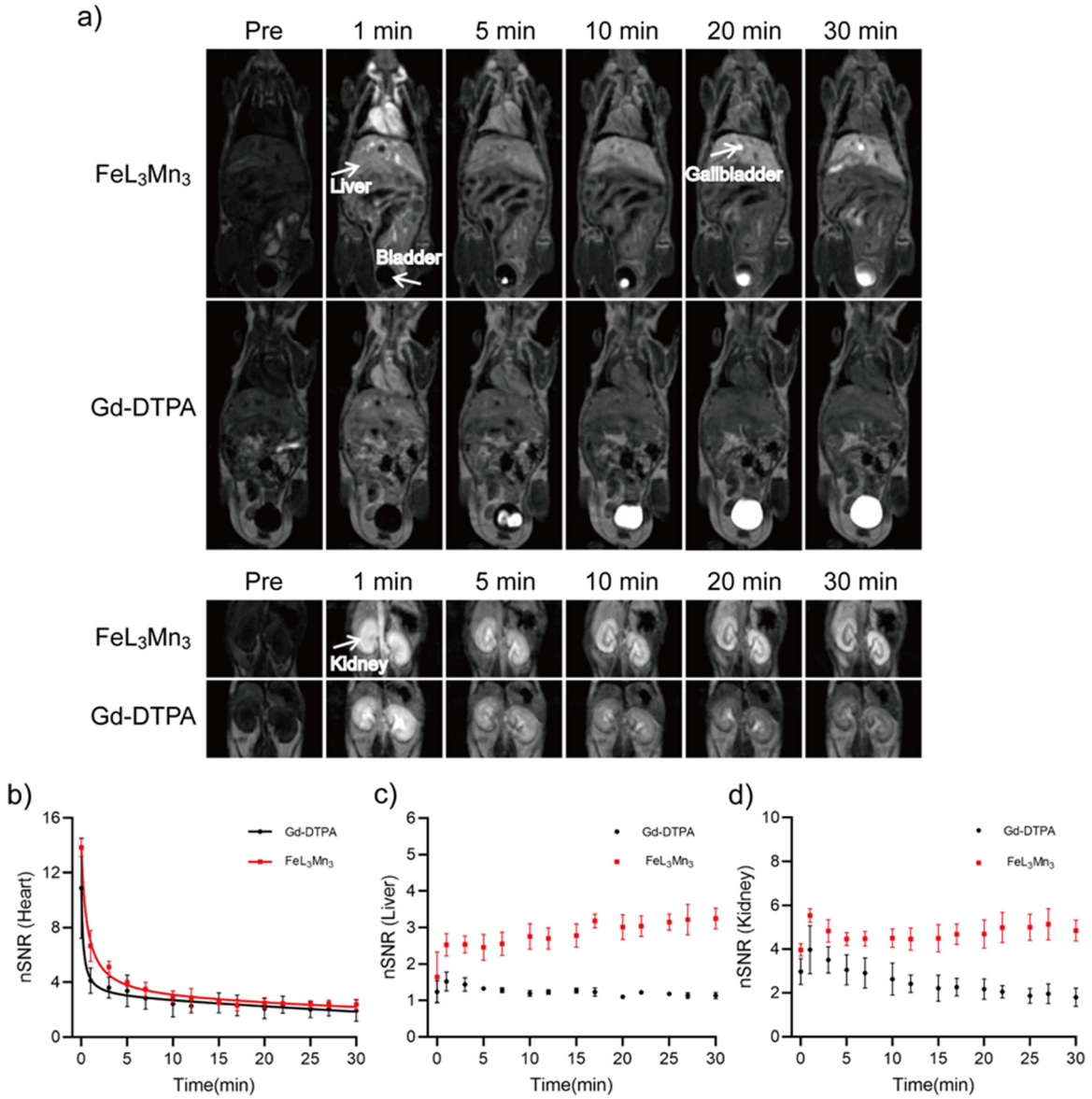

Fig. 6 MR imaging of Fe–Mn metallostar and Gd-DTPA. (a) Representative Coronal T_1-weighted MR images of Swiss mise obtained prior, 1, 5, 10, 20 and 30 min after intravenous injection of Fe–Mn metallostar (25 μmol kg^{-1}) and Gd-DTPA (100 μmol kg^{-1}), respectively. (b)–(d) The normalized SNR (nSNR) time course in the heart (b), liver (c), and kidneys (d) following CAs injection; N = 3, error bars represent standard error of the mean; the biexponential model: $\mathrm{nSNR}(t) = A\exp(-\alpha t) + B\exp(-\beta t)$.

liver, and kidney compared to Gd-DTPA, with a higher nSNR value measured during imaging time. The plasma pharmacokinetics of Fe–Mn Metallostar, estimated based on Fig. 6(b), indicate that Fe–Mn metallostar has a similar plasma pharmacokinetic to Gd-DTPA as a typical biexponential plasma clearance with a half-life of distribution as $t_{1/2,\alpha} = 0.56 \pm 0.14$ min and a half-life of elimination as $t_{1/2,\beta} = 25.71 \pm 0.69$ min. Importantly, the highly negatively charged anion nature of Fe–Mn metallostar may potentially enable tumor accumulation despite its rapid blood clearance due to the tumor's unique pathophysiological microenvironment. However, further *in vivo* studies are still needed to validate this hypothesis experimentally.

Experimental

Materials and apparatus

All experiments were executed in accordance with the Guidelines for Care and Use of Laboratory Animals and were approved by the Ethics Committee of North Sichuan Medical College (NSMC, Appl. No. 202155). Iron(III) acetylacetonate ($Fe(acac)_3$) was purchased from ACROS (New jersey, USA). Titanium(IV) oxide acetylacetonate ($TiO(acac)_2$) was purchased from Alfa-Asia (Shanghai, China). 1,3-Diphenylisobenzofuran (DPBF) was purchased from Macklin (Shanghai, China). Cell counting Kit-8 (CCK-8) and calcein/PI cell viability/cytotoxicity assay kit were purchased from beyotime (Shanghai, China). Ultrapure water in all experiments was obtained using an

ultrapure purification system. High resolution mass spectroscopy (HRMS) was performed on an Agilent QTOF 6500. The Mn concentrations were determined using an inductively coupled plasma mass spectrometry (ICP-MS, PerkinElmer Nexion 350×, USA) system. The zeta potential was determined with dynamic light scattering (DLS, Malvern Zetasizer Nano ZS 90, UK).

Preparation of metallostars

The synthetic route for MnL was derived from a previous work.[36] Next, the MnL (149.4 mg, 0.20 mmol) was dissolved in pure water (10 mL), and the pH of the ML solution was adjusted to ~9.0 through the addition of NaOH solution (1 M). $Fe(acac)_3$ (31.9 mg, 0.09 mmol; acac = acetylacetonate) dissolved in CH_2Cl_2 (10 mL) was added to the above solution and the solution was stirred for 12 h under a N_2 atmosphere. The unreacted $Fe(acac)_3$ was repeatedly extracted (2–3 times) with CH_2Cl_2, and then the CH_2Cl_2 layer was removed. After lyophilization, the crude product was obtained. The crude product was redissolved in pure water (5 mL) and the pH of the solution was adjusted carefully to ~8.5 with NaOH solution (1 M). The complex was then precipitated with isopropanol (40 mL) and the purplish-black solid product was obtained by centrifugation and drying. Yield: 74%. HRMS *m*/*z*: for $C_{51}H_{48}Mn_3FeN_6O_{30}$, calcd: 1455.0684 $[M + 10H]^+$; found: 1455.0683 $[M + 10H]^+$. The TiL_3Mn_3 was prepared with some slight modifications. Briefly, $TiO(acac)_2$ (6.0 mg, 0.023mmol) were added to the ML (49.8 mg, 0.067 mmol) aqueous solution. The TiL_3Mn_3 was synthesized according to the procedures above, and finally the orange-red solid product was obtained by precipitation with acetone. Yield: 89%. HRMS *m*/*z*: for $C_{51}H_{48}Mn_3TiN_6O_{30}$, calcd: 1446.0741 $[M + 9H]^+$; found: 1446.0740 $[M + 9H]^+$.

Relaxivity

Relaxivities of MnL, FeL_3Mn_3 and TiL_3Mn_3 were measured with a 0.47 T NMR contrast agent relaxation rate analyzer (PQ001-20-015V, Shanghai Newmag Electronic Technology Co., Ltd). Sample solutions (in HEPES buffer, pH = 7.4, 0.1 M) with different manganese ion concentrations (0.0625, 0.125, 0.25, 0.5 and 1.0 mM) were prepared first. Longitudinal (T_1) relaxation and transverse (T_2) relaxation were acquired *via* an IR (inversion recovery) sequence and a CPMG (Carr–Purcell–Meiboon–Gill) pulse sequence, respectively. Then, the slope of the linear fit of manganese ion concentrations with T_1 and T_2 relaxation times were used for calculating the longitudinal (r_1) and transverse (r_2) relaxivities.

Photothermal performances of Fe–Mn metallostar

The temperature elevation of Fe–Mn metallostar solutions (0.3 mL, in HEPES buffer, pH = 7.4, 0.1 M) under 808 nm laser irritation (VCL-808nmM1-7W, China) was measured at different concentrations (0, 0.125, 0.25, 0.5 and 1 mM with a power density of 2 W cm^{-2}) and at different laser power densities (1.0, 1.5, 2.0 and 2.5 W cm^{-2} with a concentration of 0.5 mM). The irritation time was 10 min and all the temperature changes were monitored by infrared thermography (Fotric226s, China) every 20 s. The PCE of the Fe–Mn metallostar was detected by irradiating (808 nm, 2 W cm^{-2}) the sample solution (0.3 mL, in HEPES buffer, pH = 7.4, 0.1 M) of 0.25 mM for 10 min and then cooling for 10 min. To evaluate the photostability of FeL_3Mn_3 under laser irritation, a 0.25 mM Fe–Mn metallostar solution (0.3 mL, in HEPES buffer, pH = 7.4, 0.1 M) underwent four laser (808 nm, 2.0 W cm^{-2}) on/off cycles. In each cycle, the laser was turned on to irritate the Fe–Mn metallostar and turned off for 10 min, respectively, and the absorption spectrum was measured before and after laser irritation.

Reactive oxygen species ($^1O_2$) detection

The $^1O_2$ detection of FeL_3Mn_3 was performed using 1,3-diphenylbenzofuran (DPBF) as a probe. 1.5 mL of DPBF solution (40 μM, dissolved in ethanol) was mixed with 1.5 mL of Fe–Mn metallostar solution (160 μM, dissolved in water), irritated with an 808 nm laser (1.5 W cm^{-2}), and the absorbance changes of DPBF at 410 nm were recorded using a UV-Vis spectrophotometer (UV-1900i, Japan) every 2 min.

In vitro cytotoxicity assay

BxPC-3 cells were seeded in 96-well plates (100 μL, 1×10^4 cells per well) and incubated in RPMI-1640 culture medium with 10% (v/v) fetal bovine serum and 1% (v/v) streptomycin/penicillin at 37 °C in 5% CO_2 for 24 h. Afterwards, each group was co-incubated with Fe–Mn metallostar at different concentrations (0, 31.25, 62.5, 125, 250 and 500 μM, respectively) for another 24 h. After washing with PBS, the fresh medium (100 μL) containing Cell Counting Kit-8 (CCK-8) solution (10 μL per well) was added to each well and the absorbance of each well was measured at 450 nm using a multifunctional microplate reader (Varioskan LUX, Singapore) after 1 h of incubation to calculate cell viability.

In vitro phototherapy

To evaluate photocytotoxicity, BxPC-3 cells seeded in 96-well plates (100 μL, 1×10^4 cells per well) were incubated at 37 °C in 5% CO_2 for 24 h. Afterwards, various concentrations of Fe–Mn metallostar (0, 31.25, 62.5, 125, 250 and 500 μM, respectively) were incubated with cells for 4 h and then each well was irritated with an 808 nm laser (2.0 W cm^{-2}) for 10 min. Subsequently, the cells were incubated continuously for another 24 h. Cell survival was calculated using a standard CCK-8 assay. Two control experiments were conducted to further investigate the relative contributions of photothermal therapy and photodynamic therapy to the cytotoxicity. For PDT only: all the experiments were the same as the above and BxPC-3 cells were irritated with NIR laser (808 nm, 2.0 W cm^{-2}, 10 min) at 4 °C to suppress temperature elevation. For PTT only: all the experiments were the same as the above and BxPC-3 cells were co-incubated with a ROS scavenger Vitamin C (0.5 mM) to exclude the PDT effect, followed by NIR (808 nm, 2.0 W cm^{-2}) irritation for 10 min.

Live and dead cell assay

BxPC-3 cells were plated in a confocal Petri dish (1 mL, 1×10^5 cells per dish) and incubated at 37 °C in 5% CO_2 for 24 h. Then, BxPC-3 cells were divided into four groups: (1) control, (2) laser irritation only (808 nm, 2 W cm^{-2}, 10 min), (3) Fe–Mn metallostar only (500 μM) and (4) Fe–Mn metallostar (500 μM) + laser irritation (808 nm, 2 W cm^{-2}, 10 min). After 24 h of co-cultivation, different treatment groups were co-stained with the AM/PI staining method for 30 min, and then cell imaging was performed using an Olympus laser scanning confocal microscope.

MR imaging protocol

Swiss mice (Male, 20–25 g, purchased from Laboratory Animal Center of NSMC, Sichuan, China) were maintained under anesthesia by inhalation of isoflurane (RWD Life Science, Shenzhen, China) at an anesthetic concentration of 0.8–1.5% and 20–30 mL O_2 per kg. Baseline imaging was performed using a system-equipped mice coil, under a 3.0 T MR scanner (Discovery MR750, GE Medical System, Milwaukee, WI) and multi-slice 2D T1WI-FSPGR sequence, followed by injection of FeL_3Mn_3 (25 μmol kg^{-1}) or Gd-DTPA (100 μmol kg^{-1}) to obtain contrast-enhanced images of mice (n = 3, per group). The MRI parameters were as follows: TE = 2.3 ms, TR = 6.1 ms, FA = 30°, FOV = 9.0 × 6.3 cm^2, matrix size = 256 × 256, slices = 40, slice thickness = 1.0 mm, NEX = 1.00, and bandwidth = 62.50 Hz. The normalized signal-to-noise ratio (nSNR) was calculated according to the formula: $nSNR = SNR_{post}/SNR_{pre}$ and $SNR = SI/SD_{air}$, where SI stands for the signal intensity and SD_{air} stands for the standard deviation of the noise estimated from the background air.

Conclusions

The study presented here demonstrates a unique multifunctional Mn(II)-metallostar based on coordination-driven self-assembly, in which the metallostar with the core of Fe(III)-catechol exhibits high per Mn relaxivity and good NIR-irritable PTT/PDT effects. Cellular phototoxicity studies confirmed the good biosafety and phototherapeutic effects of FeL_3Mn_3. The *in vivo* MRI study on mice demonstrated that a low-dose of Fe–Mn metallostar (25 μmol kg^{-1}) can provide superior contrast enhancement compared to Gd-DTPA (100 μmol kg^{-1}) with rapid blood clearance and a mixed route of hepatobiliary and renal excretion, which considerably reduces the potential side effects of the metallostar complex. Our findings may provide useful guidance for the future development of non-gadolinium-based metallostars with attractive theranostic potential.

Abbreviations

AM	Acetoxymethyl ester
Cas	Contrast agents
CCK-8	Cell counting kit-8
CE	Contrast enhanced
CPMG	Carr–Purcell–Meiboon–Gill
DLS	Dynamic light scattering
DPBF	1,3-Diphenylisobenzofuran
DTPA	Diethylenetriaminetetraacetic acid
EDTA	Ethylenediaminetetraacetic acid
GBCAs	Gadolinium-based contrast agents
HRMS	High-resolution mass spectrometry
ICP-MS	Inductively coupled plasma mass spectrometry
IR	Inversion recovery
LMCT	Ligand-to-metal charged transfer
MRI	Magnetic resonance imaging
NIR	Near-infrared
NMR	Nuclear magnetic resonance
nSNR	Normalized signal-to-noise ratio
NSF	nephrogenic systemic fibrosis
PDT	Photodynamic therapy
PI	Propidium iodide
PTT	Photothermal therapy
ROS	Reactive oxidative species

Author contributions

The manuscript was written through contributions of all authors. H.-Y. W. and J. Z. conceived the project. J. Z., H.-Y. W. and Z.-H. L. designed the experiments. H.-Y. W. and Z.-H. L. conducted the synthesis and characterization of all compounds. H.-Y. W., Y. X., Y. L. and Z.-H. H. carried out imaging study. J. Z. and H.-Y. W. prepared the manuscript. All authors have approved the final version of the manuscript. All authors have given approval to the final version of the manuscript.

Conflicts of interest

The authors declare no competing financial interest.

Acknowledgements

The authors acknowledge the financial support of the National Natural Science Foundation of China (81671675, 21172025), and the Science and Technology Project of Municipal School Strategic Cooperation, Nanchong (NSMC20170101, 18SXHZ0091,18SXHZ0379, 20SXQT0180).

References

1 V. S. Vassiliou, D. Cameron, S. K. Prasad and P. D. Gatehouse, Magnetic resonance imaging: Physics basics for the cardiologist, *JRSM Cardiovasc Dis*, 2018, 7, 204800 4018772237.
2 E. Kanal, Gadolinium based contrast agents (GBCA): Safety overview after 3 decades of clinical experience, *Magn. Reson. Imaging*, 2016, **34**, 1341–1345.

3 R. B. Lauffer, Paramagnetic metal complexes as water proton relaxation agents for NMR imaging: theory and design, *Chem. Rev.*, 1987, **87**, 901–927.
4 P. Caravan, J. J. Ellison, T. J. McMurry and R. B. Lauffer, Gadolinium(III) Chelates as MRI Contrast Agents: Structure, Dynamics, and Applications, *Chem. Rev.*, 1999, **99**, 2293–2352.
5 K. Hanaoka, A. J. Lubag, A. Castillo-Muzquiz, T. Kodadek and A. D. Sherry, The detection limit of a Gd^{3+}-based T_1 agent is substantially reduced when targeted to a protein microdomain, *Magn. Reson. Imaging*, 2008, **26**, 608–617.
6 L. M. Manus, D. J. Mastarone, E. A. Waters, X. Q. Zhang, E. A. Schultz-Sikma, K. W. Macrenaris, D. Ho and T. J. Meade, Gd(III)-nanodiamond conjugates for MRI contrast enhancement, *Nano Lett.*, 2010, **10**, 484–489.
7 T. Barrett, H. Kobayashi, M. Brechbiel and P. L. Choyke, Macromolecular MRI contrast agents for imaging tumor angiogenesis, *Eur. J. Radiol.*, 2006, **60**, 353–366.
8 Z. Zhang, M. T. Greenfield, M. Spiller, T. J. McMurry, R. B. Lauffer and P. Caravan, Multilocus binding increases the relaxivity of protein-bound MRI contrast agents, *Angew. Chem., Int. Ed.*, 2005, **44**, 6766–6769.
9 P. Caravan, G. Parigi, J. M. Chasse, N. J. Cloutier, J. J. Ellison, R. B. Lauffer, C. Luchinat, S. A. McDermid, M. Spiller and T. J. McMurry, Albumin binding, relaxivity, and water exchange kinetics of the diastereoisomers of MS-325, a gadolinium(III)-based magnetic resonance angiography contrast agent, *Inorg. Chem.*, 2007, **46**, 6632–6639.
10 Y. Li, M. Beija, S. Laurent, L. V. Elst, R. N. Muller, H. T. T. Duong, A. B. Lowe, T. P. Davis and C. Boyer, Macromolecular Ligands for Gadolinium MRI Contrast Agents, *Macromolecules*, 2012, **45**, 4196–4204.
11 M. Younis, V. Darcos, C. Paniagua, P. Ronjat, L. Lemaire, B. Nottelet, X. Garric, Y. Bakkour, J. H. El Nakat and J. Coudane, MRI-visible polymer based on poly(methyl methacrylate) for imaging applications, *RSC Adv.*, 2016, **6**, 5754–5760.
12 T. R. Berki, J. Martinelli, L. Tei, H. Willcock and S. J. Butler, Polymerizable Gd(III) building blocks for the synthesis of high relaxivity macromolecular MRI contrast agents, *Chem. Sci.*, 2021, **12**, 3999–4013.
13 Z. Xiong, Y. Wang, J. Zhu, Y. He, J. Qu, C. Effenberg, J. Xia, D. Appelhans and X. Shi, Gd-Chelated poly(propylene imine) dendrimers with densely organized maltose shells for enhanced MR imaging applications, *Biomater. Sci.*, 2016, **4**, 1622–1629.
14 C. Sun, H. Lin, X. Gong, Z. Yang, Y. Mo, X. Chen and J. Gao, DOTA-Branched Organic Frameworks as Giant and Potent Metal Chelators, *J. Am. Chem. Soc.*, 2020, **142**, 198–206.
15 S. Zhang, V. Lloveras, D. Pulido, F. Liko, L. F. Pinto, F. Albericio, M. Royo and J. Vidal-Gancedo, Radical Dendrimers Based on Biocompatible Oligoethylene Glycol Dendrimers as Contrast Agents for MRI, *Pharmaceutics*, 2020, **12**, 772.
16 J. Bryson, J. W. Reineke and T. M. Reineke, Macromolecular Imaging Agents Containing Lanthanides: Can Conceptual Promise Lead to Clinical Potential?, *Macromolecules*, 2012, **45**, 8939–8952.
17 V. Comblin, D. Gilsoul, M. Hermann, V. Humblet, V. Jacques, M. Mesbahi, C. Sauvage and J. F. Desreux, Designing new MRI contrast agents: a coordination chemistry challenge, *Coord. Chem. Rev.*, 1999, **185–186**, 451–470.
18 L. Moriggi, A. Aebischer, C. Cannizzo, A. Sour, A. Borel, J. C. Bunzli and L. Helm, A ruthenium-based metallostar: synthesis, sensitized luminescence and (1)H relaxivity, *Dalton Trans.*, 2009, 2088–2095, DOI: 10.1039/b818599a.
19 M. Ceulemans, E. Debroye, L. Vander Elst, W. De Borggraeve and T. N. Parac-Vogt, Luminescence and Relaxometric Properties of Heteropolymetallic Metallostar Complexes with Selectively Incorporated Lanthanide(III) Ions, *Eur. J. Inorg. Chem.*, 2015, 4207–4216.
20 P. Marckmann, L. Skov, K. Rossen, A. Dupont, M. B. Damholt, J. G. Heaf and H. S. Thomsen, Nephrogenic systemic fibrosis: suspected causative role of gadodiamide used for contrast-enhanced magnetic resonance imaging, *J. Am. Soc. Nephrol.*, 2006, **17**, 2359–2362.
21 J.-M. Idée, N. Fretellier, C. Robic and C. Corot, The role of gadolinium chelates in the mechanism of nephrogenic systemic fibrosis: a critical update, *Crit. Rev. Toxicol.*, 2014, **44**, 895–913.
22 T. Kanda, T. Fukusato, M. Matsuda, K. Toyoda, H. Oba, J. Kotoku, T. Haruyama, K. Kitajima and S. Furui, Gadolinium-based Contrast Agent Accumulates in the Brain Even in Subjects without Severe Renal Dysfunction: Evaluation of Autopsy Brain Specimens with Inductively Coupled Plasma Mass Spectroscopy, *Radiology*, 2015, **276**, 228–232.
23 J. Ramalho, R. C. Semelka, M. Ramalho, R. H. Nunes, M. AlObaidy and M. Castillo, Gadolinium-Based Contrast Agent Accumulation and Toxicity: An Update, *AJNR Am. J. Neuroradiol.*, 2016, **37**, 1192–1198.
24 V. M. Runge, Critical Questions Regarding Gadolinium Deposition in the Brain and Body After Injections of the Gadolinium-Based Contrast Agents, Safety, and Clinical Recommendations in Consideration of the EMA's Pharmacovigilance and Risk Assessment Committee Recommendation for Suspension of the Marketing Authorizations for 4 Linear Agents, *Invest. Radiol.*, 2017, **52**, 317–323.
25 E. M. Gale, I. P. Atanasova, F. Blasi, I. Ay and P. Caravan, A Manganese Alternative to Gadolinium for MRI Contrast, *J. Am. Chem. Soc.*, 2015, **137**, 15548–15557.
26 D. Ndiaye, M. Sy, A. Pallier, S. Meme, I. de Silva, S. Lacerda, A. M. Nonat, L. J. Charbonniere and E. Toth, Unprecedented Kinetic Inertness for a Mn(2+)-Bispidine Chelate: A Novel Structural Entry for Mn(2+)-Based Imaging Agents, *Angew. Chem., Int. Ed.*, 2020, **59**, 11958–11963.
27 V. L. Pecoraro, G. B. Wong and K. N. Raymond, Gallium and indium imaging agents. 2. Complexes of sulfonated catechoylamide sequestering agents, *Inorg. Chem.*, 1982, **21**, 2209–2215.
28 B. A. Borgias, S. R. Cooper, Y. B. Koh and K. N. Raymond, Synthetic, structural, and physical studies of titanium complexes of catechol and 3,5-di-*tert*-butylcatechol, *Inorg. Chem.*, 1984, **23**, 1009–1016.
29 X. Tu, S. Luo, X. Luo, Y. Zhao, L. Feng and J. Li, Metal chelate affinity to immobilize horseradish peroxidase on

functionalized agarose/CNTs composites for the detection of catechol, *Sci. China: Chem.*, 2011, **54**, 1319–1326.

30 A. Nucera, F. Carniato, Z. Baranyai, C. Platas-Iglesias and M. Botta, Characterization of the Fe(III)-Tiron System in Solution through an Integrated Approach Combining NMR Relaxometric, Thermodynamic, Kinetic, and Computational Data, *Inorg. Chem.*, 2023, **62**, 4272–4283.

31 X. Huang, X. Sun, W. Wang, Q. Shen, Q. Shen, X. Tang and J. Shao, Nanoscale metal-organic frameworks for tumor phototherapy, *J. Mater. Chem. B*, 2021, **9**, 3756–3777.

32 R. Xing, Q. Zou, C. Yuan, L. Zhao, R. Chang and X. Yan, Self-Assembling Endogenous Biliverdin as a Versatile Near-Infrared Photothermal Nanoagent for Cancer Theranostics, *Adv. Mater.*, 2019, **31**, 1900822.

33 L. Zhao, Y. Liu, R. Xing and X. Yan, Supramolecular Photothermal Effects: A Promising Mechanism for Efficient Thermal Conversion, *Angew. Chem., Int. Ed.*, 2020, **59**, 3793–3801.

34 S. Li, W. Zhang, R. Xing, C. Yuan, H. Xue and X. Yan, Supramolecular Nanofibrils Formed by Coassembly of Clinically Approved Drugs for Tumor Photothermal Immunotherapy, *Adv. Mater.*, 2021, **33**, 2100595.

35 R. Chang, Q. Zou, L. Zhao, Y. Liu, R. Xing and X. Yan, Amino-Acid-Encoded Supramolecular Photothermal Nanomedicine for Enhanced Cancer Therapy, *Adv. Mater.*, 2022, **34**, 2200139.

36 C. Wu, T. Chen, L. Deng, Q. Xia, C. Chen, M. Lan, Y. Pu, H. Tang, Y. Xu, J. Zhu, C. Xu, C. Shen and X. Zhang, Mn(II) chelate-coated superparamagnetic iron oxide nanocrystals as high-efficiency magnetic resonance imaging contrast agents, *Nanoscale Adv.*, 2020, **2**, 2752–2757.

37 L. K. Charkoudian and K. J. Franz, Fe(III)-Coordination Properties of Neuromelanin Components: 5,6-Dihydroxyindole and 5,6-Dihydroxyindole-2-carboxylic Acid, *Inorg. Chem.*, 2006, **45**, 3657–3664.

38 M. Albrecht, S. Mirtschin, M. de Groot, I. Janser, J. Runsink, G. Raabe, M. Kogej, C. A. Schalley and R. Fröhlich, Hierarchical Assembly of Helicate-Type Dinuclear Titanium(IV) Complexes, *J. Am. Chem. Soc.*, 2005, **127**, 10371–10387.

39 G. Liang, J. Han and D. Xing, Precise Tumor Photothermal Therapy Guided and Monitored by Magnetic Resonance/Photoacoustic Imaging using A Safe and pH-Responsive Fe(III) Complex, *Adv. Healthcare Mater.*, 2021, **10**, e2001300.

40 X. Zhang, Y. Lin and R. J. Gillies, Tumor pH and its measurement, *J. Nucl. Med.*, 2010, **51**, 1167–1170.

41 D. H. Powell, O. M. N. Dhubhghaill, D. Pubanz, L. Helm, Y. S. Lebedev, W. Schlaepfer and A. E. Merbach, Structural and Dynamic Parameters Obtained from ^{17}O NMR, EPR, and NMRD Studies of Monomeric and Dimeric Gd^{3+} Complexes of Interest in Magnetic Resonance Imaging: An Integrated and Theoretically Self-Consistent Approach1, *J. Am. Chem. Soc.*, 1996, **118**, 9333–9346.

42 E. M. Gale, J. Zhu and P. Caravan, Direct measurement of the Mn(II) hydration state in metal complexes and metalloproteins through ^{17}O NMR line widths, *J. Am. Chem. Soc.*, 2013, **135**, 18600–18608.

43 D. K. Roper, W. Ahn and M. Hoepfner, Microscale Heat Transfer Transduced by Surface Plasmon Resonant Gold Nanoparticles, *J. Phys. Chem. C*, 2007, **111**, 3636–3641.

44 T. Entradas, S. Waldron and M. Volk, The detection sensitivity of commonly used singlet oxygen probes in aqueous environments, *J. Photochem. Photobiol., B*, 2020, **204**, 111787.

45 C. Sui, R. Tan, Y. Chen, G. Yin, Z. Wang, W. Xu and X. Li, MOFs-Derived Fe–N Codoped Carbon Nanoparticles as O_2-Evolving Reactor and ROS Generator for CDT/PDT/PTT Synergistic Treatment of Tumors, *Bioconjugate Chem.*, 2021, **32**, 318–327.

46 J. Y. Chen, K. K. Wen, H. Chen, S. Jiang, X. X. Wu, L. Lv, A. D. Peng, S. M. Zhang and H. Huang, Achieving High-Performance Photothermal and Photodynamic Effects upon Combining D–A Structure and Nonplanar Conformation, *Small*, 2020, **16**, e2000909.

47 J. R. Deng, M. Q. Yang, C. Li, G. Y. Liu, Q. Sun, X. G. Luo and F. S. Wu, Single molecular-based nanoparticles with aggregation-induced emission characteristics for fluorescence imaging and efficient cancer phototherapy, *Dyes Pigm.*, 2021, **187**, 7.